

PAPER • OPEN ACCESS

$\text{Na}_2\text{Fe}(\text{C}_2\text{O}_4)(\text{HPO}_4)$: a promising new oxalate-phosphate based mixed polyanionic cathode for Li/Na ion batteries

To cite this article: Atin Pramanik *et al* 2021 *J. Phys. Mater.* **4** 024004

View the [article online](#) for updates and enhancements.



240th ECS Meeting ORLANDO, FL

Orange County Convention Center Oct 10-14, 2021

Abstract submission due: April 9

SUBMIT NOW



PAPER

OPEN ACCESS

RECEIVED
3 November 2020REVISED
21 January 2021ACCEPTED FOR PUBLICATION
12 February 2021PUBLISHED
25 February 2021

Original content from this work may be used under the terms of the [Creative Commons Attribution 4.0 licence](#).

Any further distribution of this work must maintain attribution to the author(s) and the title of the work, journal citation and DOI.



Na₂Fe(C₂O₄)(HPO₄): a promising new oxalate-phosphate based mixed polyanionic cathode for Li/Na ion batteries

Atin Pramanik¹ , Alasdair J Bradford¹ , Stephen L Lee² , Philip Lightfoot¹ and A Robert Armstrong¹

¹ School of Chemistry, University of St Andrews, St Andrews, Fife KY16 9ST, United Kingdom

² School of Physics, University of St Andrews, St Andrews, Fife KY16 9SS, United Kingdom

E-mail: pl@st-andrews.ac.uk and ara@st-andrews.ac.uk

Keywords: Na₂Fe(C₂O₄)(HPO₄), oxalate-phosphate mixed polyanion, sodium-ion battery, lithium-ion battery, cathode

Supplementary material for this article is available [online](#)

Abstract

The new iron-based mixed polyanionic material Na₂Fe(C₂O₄)(HPO₄) has been synthesized by a hydrothermal technique. The compound contains four Na sites with a three-dimensional crystal structure. This compound shows promising reversible Li and Na insertion properties as a cathode material. The redox potentials observed were ~3.2 V (vs Li⁺/Li) for the Li-ion cell and ~3.1 V (vs Na⁺/Na) for the Na-ion cell with Fe^{2+/3+} redox reactions. The reversible electrode operation was found to deliver 71 and 104 mAh g⁻¹ specific capacities in Li and Na half cells, respectively. This present study reveals promising performance from a mixed oxalate-phosphate based polyanionic material and opens up further possibilities for materials discovery.

1. Introduction

In recent years, due to the rapid growth of sustainable and renewable energies such as solar, wind, tidal, etc advanced energy storage amenities are also undergoing fast development [1, 2]. Among a range of energy storage devices, rechargeable batteries represent the most promising candidate. In this aspect, high energy density is needed for practical portable applications. In order to meet the current societal demand, there is a considerable need for the development of suitable high energy density electrode materials with higher specific capacity [3].

Until now, rechargeable lithium-ion batteries (LIBs) have been the dominant power sources for use in mobile electronic devices, because of their high energy and power densities, desirable cycle life, environmentally friendly, etc [4]. However, the rapid growth in the use of LIBs, particularly for automotive applications, has led to concerns over lithium supply. Growing energy demands, combined with limited lithium abundance and non-uniform global distribution (much of it in South America) poses a real challenge to meet future demands. Sodium-ion batteries (NIBs) are the most promising alternative technology to LIBs, especially for large-scale energy storage from intermittent and renewable sources and smart grid applications, given the low cost and widespread natural abundance of sodium. Despite the lower materials costs, the electrochemical performance of NIBs is still inferior to state-of-the-art LIBs, with limited sodium storage capacity and lower working potentials.

In the search for new positive electrodes for NIBs, recently several layered transition metal (TM) oxides have been investigated, such as NaTMO₂ [5], in addition to a range of polyanionic materials (e.g. phosphates, sulfates, silicates, etc such as olivine type (NaTMPO₄) [6], and NASICON type (Na_xM₂(PO₄)₃; M = V, Ti, x = 1, 2, 3) [7]. Generally, oxides have a higher theoretical capacity (~150 mAh g⁻¹) with a one-electron redox reaction, though the valences of TMs vary between +3 and +4. On the other hand, due to formation of strong covalent bonds, polyanionic compounds exhibit enhanced stability, which also improves safety characteristics. Polyanionic cathodes generally display higher voltages as a result of the inductive effect, and have become an attractive option for high-voltage electrode materials [8]. Recently, research on polyanion based cathodes has concentrated on phosphate and sulfate-based materials for NIB applications [9].

In the search for new cathode materials our group has developed TM oxalates as potential cathode materials for NIB/LIBs. Oxalic acid ($pK_a = 1.25/4.14$) is a relatively strong acid, intermediate between H_2SO_4 ($pK_a = -3/1.99$) and H_3PO_4 ($pK_a = 2.15/7.20/12.32$). This implies that the electronic inductive effect on the d-states of the TM ions of oxalate group should be analogous to $(SO_4)^{2-}$ and $(PO_4)^{3-}$. As a result, oxalate shows a similar range of redox potentials to phosphate and sulfate [10]. Additionally, its conjugate base, $(C_2O_4)^{2-}$, is a versatile anion that can readily co-ordinate with the metal centers via oxygen atoms. Being a multidentate ligand (monodentate, bidentate, tridentate, or tetradentate), oxalate anions form chains, layers, or three-dimensional structures with metal centers [11]. As a result of these advantages of oxalates our group has recently developed oxalate based (e.g. $Na_2Fe_2(C_2O_4)_3 \cdot 2H_2O$ [12], $Na_2Fe(C_2O_4)F_2$ [10], and $Li_2Fe(C_2O_4)_2$) [13] polyanionic cathodes for NIB/LIB application. The favourable working potentials and satisfactory capacities of such polyanionic materials offer high output energy densities with structural stability, making them very stable during long term cycling.

Recent advances in polyanionic redox chemistry have included using different types of polyanion within the same material. These mixed polyanionic combinations can lead to rich structural diversity as well as multiple electron redox processes leading to robust electrochemical performance. In addition, a combination of different polyanions can be beneficial in tuning the redox potential by structural diversity and varying degrees of inductive effect. In recent years, research for NIBs has mainly focussed on mixed phosphate-based positive electrode materials such as $Na_4Co_3(PO_4)_2P_2O_7$ [14], $Na_7V_4(P_2O_7)_4PO_4$ [15], $Na_4Mn_3(PO_4)_2P_2O_7$ [16, 17], etc). However there are only a handful of examples reported on systems containing different mixed polyanions such as $(NH_4)_{0.94}Li_{0.06}FePO_4NO_3$ [18], $Na_3MnPO_4CO_3$ [19], $Na_2Fe(C_2O_4)SO_4 \cdot H_2O$ [20], and $K_{2.5}[(VO)_2(HPO_4)_{1.5}(PO_4)_{0.5}(C_2O_4)] \cdot 4.5H_2O$ [21].

Inspired by the above considerations, we synthesized the novel iron-based mixed oxalate phosphate $Na_2Fe(C_2O_4)(HPO_4)$ as a promising cathode material for rechargeable LIB/NIB application with a theoretical capacity of $\sim 98 \text{ mAh g}^{-1}$. Here, we report a simple hydrothermal synthesis, structure determination, physical characterization, and detailed electrochemical behaviour. The compound displays a $Fe^{2+/3+}$ redox reaction during the electrochemical process. Additionally, no crystallographic changes are observed after cycling and the material exhibits promising long-term reversible lithium and sodium insertion.

2. Experimental

2.1. Synthesis and characterization

Simple single-step hydrothermal synthesis was performed to obtain single crystals of the title compound. In this procedure, as obtained iron (II) chloride hexahydrate (99%, Alfa Aesar), disodium hydrogen phosphate ($\geq 99.0\%$, Merck), and oxalic acid dihydrate (98%, Alfa Aesar) were mixed in the ratio 1:3:2 (1 corresponding to 10 mmol) in a 23 ml Teflon-lined autoclave with 3 ml of distilled water, sealed and placed in an oven at 160°C for 3 d. The autoclave was then extracted from the oven and cooled to room temperature. The contents were decanted onto filter paper and washed several times with deionised water and acetone. The orange single-crystalline product was then dried in an oven at 60°C for 4 h.

2.2. Single crystal x-ray diffraction (SXRD)

A fine orange single crystal was selected and mounted on nylon loops in inert oil. The SXRD data were acquired using $Mo\ K\alpha$ radiation ($\lambda = 0.71073 \text{ \AA}$) at 173 K, on a Rigaku SCX Mini diffractometer. The data processing was carried out using Rigaku CrystalClear 2.0. SHELX-2014 incorporated in the WinGX program was used to solve the crystal structure by direct methods followed by further refinement [22, 23]. Absorption corrections were performed semi-empirically from equivalent reflections using multi scans data. All non-hydrogen atoms were refined anisotropically. The atomic positions of the material are shown in table S1 (available online at stacks.iop.org/JPMATER/4/024004/mmedia).

2.3. Characterization

Powder x-ray diffraction (PXRD) patterns were recorded using a Stoe STADI/P diffractometer operating in either transmission mode or Debye–Scherrer mode with $Cu\ K\alpha_1$ radiation ($\lambda = 1.5406 \text{ \AA}$) in the 2θ range $5\text{--}100^\circ$. In order to verify phase purity of the sample the datasets were refined by conventional Rietveld methods, using the GSAS package with the EXPGUI interface [23]. For this purpose, a fixed structural model, taken from the SXRD study, was used, and only lattice parameters and profile parameters were refined, including the modelling of some preferred orientation using the spherical harmonics model [24]. A JEOL JSM-6700F scanning electron microscope (SEM) was used to record the morphological features and elemental mapping of the sample. The instrument was also equipped with a field emission gun electron source. Secondary electron images were recorded with a tungsten filament electron source using an accelerating voltage of 5 kV for the hand-ground pristine sample, and 15 kV for ball-milled and composite

Table 1. Crystallographic data for Na₂Fe(C₂O₄)(HPO₄).

Formula	C ₄ H ₂ Fe ₂ Na ₄ O ₁₆ P ₂
Crystal system	Monoclinic
Space group	P2 ₁ /c (No. 14)
<i>a</i> , <i>b</i> , <i>c</i> (Å)	6.4728(5), 20.2103(16), 10.4712(8)
β (°)	90.745(8)
<i>V</i> (Å ³)	1369.70(18)
<i>F</i> (000)	1120
<i>R</i> ₁ , <i>wR</i> ₂ (<i>I</i> > 2σ(<i>I</i>)) ^{a,b}	0.0928, 0.2384
<i>R</i> ₁ , <i>wR</i> ₂ (all data)	0.1052, 0.2540
Goodness-of-fit on <i>F</i> ²	1.089

$$^a R_1 = \frac{\sum ||F_o| - |F_c||}{\sum |F_o|}$$

$$^b wR_2 = (\frac{\sum [w(F_o^2 - F_c^2)^2]}{\sum wF_o^4})^{1/2}$$

samples. For atomic number contrast imaging a retractable backscattered electron detector was used. FTIR spectroscopy was recorded using a Shimadzu IR affinity-1 FTIR spectrophotometer in the range of 400–4000 cm⁻¹. The cells were opened inside the glovebox after 15 charge/discharge cycles and the samples recovered and washed with dry dimethyl carbonate (anhydrous, 99.8% Merck). Then capillaries were filled with dried sample inside the glovebox and PXRD were recorded using Mo Kα1 radiation ($\lambda = 0.7107 \text{ \AA}$) in the 2θ range 4–40° for both NIB and LIB. Thermogravimetric analysis (TGA) was carried out on a Stanton Redcroft STA-780 simultaneous TG-DTA, under an air atmosphere at a heating ramp rate of 10 °C min⁻¹.

2.4. Magnetic characterization

A 44 mg of powdered material was packed into a polycarbonate capsule and suspended inside a polypropylene straw. This was then attached to a sample rod and lowered into a Quantum Design MPMS[®] XL for SQUID Magnetometry measurements. The powder sample at 300 K was subjected to a magnetic field of 100 Oe (0.1 T) and the sample was cooled to 2 K while the magnetic susceptibility was recorded.

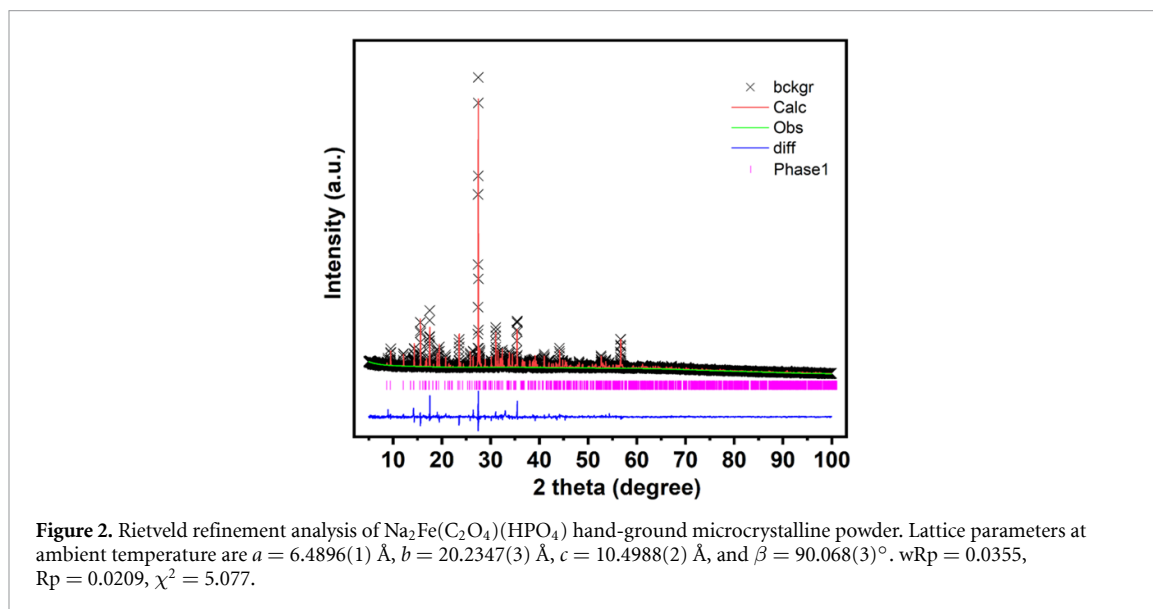
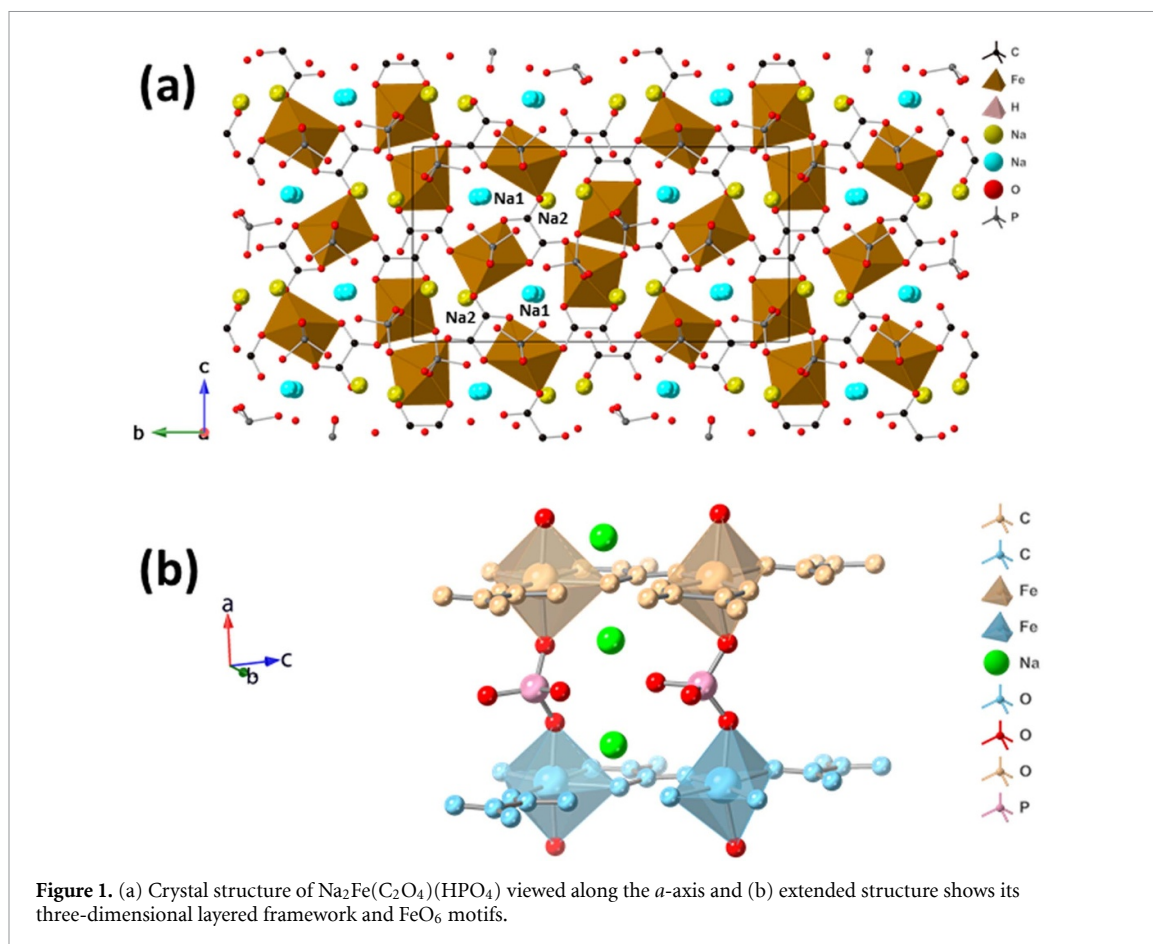
2.5. Electrochemistry

The crystalline material was the first ball milled for 1 h to form a fine powder using a Fritsch Pulverisette 8 mill. Then 0.6 g of powdered material was mixed with 0.3 g Super C65 conductive carbon black (Imerys) via ball milling for a further 30 min. The composite powder was then ground with 0.1 g polytetrafluoroethylene (PTFE) binder until a homogeneous mixture was obtained. Pellets were pressed using hand hydraulic press at 3 tonnes cm⁻². The self-standing 13 mm pellets (~0.08 mm thickness) were dried in a vacuum oven overnight and directly transferred to glovebox to use as working electrode. Typically, cathode pellet electrodes containing ~7–8 mg active material were tested in half cells using CR2325 (NRC Canada) coin cells with Na metal as the anode, 1 M NaClO₄ in propylene carbonate with 3% fluoroethylene carbonate as the electrolyte for NIB; and Li metal as the anode, LP30 (1 M LiPF₆ in ethylene carbonate: dimethyl carbonate = 1:1) as the electrolyte for LIB. The half-cells were cycled galvanostatically in the potential window of 1.7–4.3 V for NIB and 1.9–4.5 V for LIB at a rate of 10 mA g⁻¹ using a Biologic Macpile II system. The rate capability was tested by cycling at progressively increasing rates up to 100 mA g⁻¹ before returning to 10 mA g⁻¹.

3. Results and discussion

3.1. Structure

The single-crystal XRD data are shown in table 1. The structure viewed along the *a*-axis is shown in figure 1(a). This complex structure consists of distorted Fe²⁺O₆ octahedra (figure 1(a)) which are linked into triangular chains by oxalate ligands along the *c*-axis. These chains, which may be regarded as derived from the triangular layers seen in KFe(C₂O₄)F and related materials [25] are linked into layers in the *bc*-plane by surrounding hydrogen phosphate groups. These, in turn, link stacked octahedra directly along the *a*-axis and corrugate the chains through the *b*-axis (figure 1(b)). Interspersed through the structure are Na⁺ ions at four distinct crystallographic positions. These may be regarded as four or five-coordinate to oxygen ligands (assuming Na–O bond lengths to 2.6 Å), from both phosphate and oxalate moieties. Half of the Na⁺ sites are arranged along the *a*-axis, with their coordination polyhedra alternately sharing faces and edges (labelled Na1 in figure 1(a)). This channel is the prime candidate for any ion migration, with the small possibility of a secondary channel along the *b*-axis.



Rietveld refinement of the PXRD pattern from a hand-ground sample (figure 2(a)) confirmed that the sample is isostructural with the low temperature (-100°C) single-crystal XRD data. We estimate only a small amount ($\ll 5\%$) of an unidentified impurity (figure S1).

SEM images reveal that the hand-ground sample shows an average particle size of $12\text{--}20\ \mu\text{m}$ (figures 3(a) and (b)). Elemental mapping confirms that the elements Na, Fe, C, O, and P are homogeneously distributed throughout the sample (figure S2). As the particle size obtained from hand-grinding is too large for electrochemical measurements the sample was ball milled for 30 min and the particle size checked by SEM analysis.

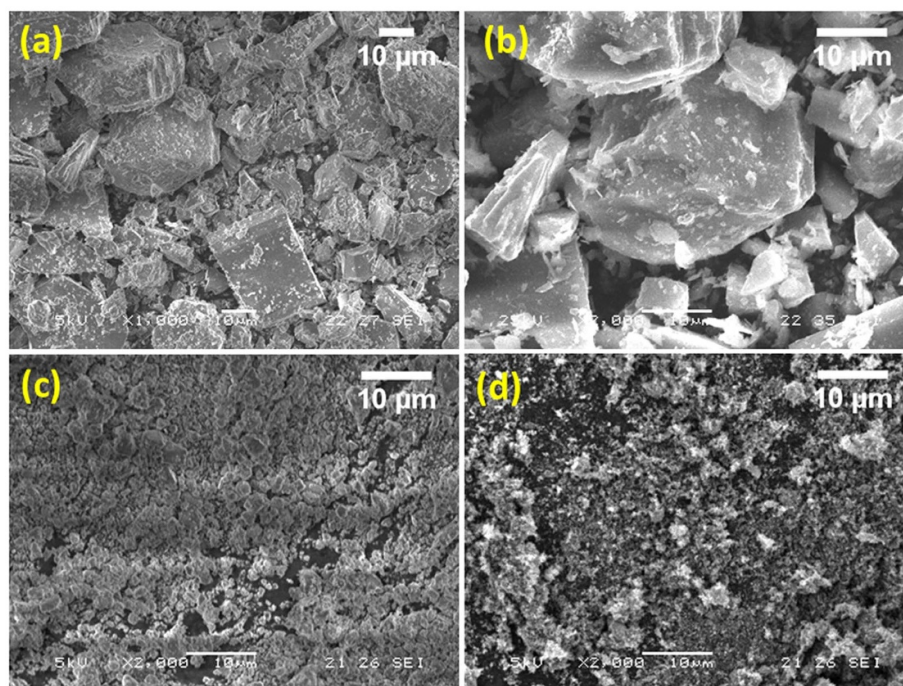


Figure 3. SEM images of $\text{Na}_2\text{Fe}(\text{C}_2\text{O}_4)(\text{HPO}_4)$ (a), (b) pristine sample, (c) ball-milled, and (d) sample and carbon C65 composite powder.

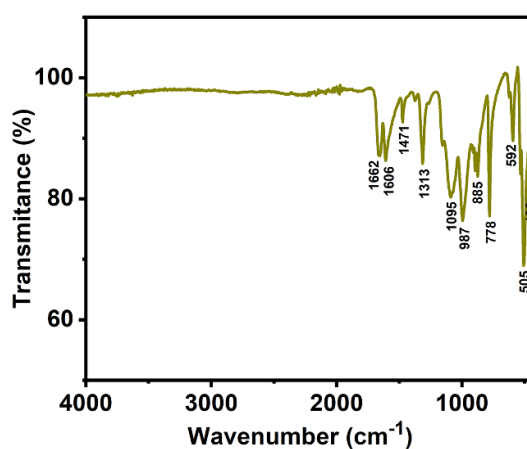


Figure 4. FTIR spectrum of pristine $\text{Na}_2\text{Fe}(\text{C}_2\text{O}_4)(\text{HPO}_4)$ powder.

This revealed that the particle size was reduced to 2–4 μm (figure 3(c)). These materials typically exhibit poor electronic conductivity hence 30 wt. % of conductive carbon C65 was added and the mixture ball-milled for a further 30 min. SEM images of the composite show that there is a homogeneous mixture of sample and carbon C65 (figure 3(c)) with reduced particle size.

The pristine $\text{Na}_2\text{Fe}(\text{C}_2\text{O}_4)(\text{HPO}_4)$ was further characterized by FTIR spectroscopy to determine coordination of atoms and to confirm the absence of H_2O or OH^- from the structure. Figure 4 confirms the absence of absorption peaks of H_2O or OH^- , in the range 3000–4000 cm^{-1} . The absorption peaks at 438, 505, 778, 885 and 1095 cm^{-1} correspond to Fe– PO_4 antisymmetric stretching, Fe–O symmetric stretching, $\delta(\text{OCO})$ bending modes, $\nu(\text{C–C})$ stretching vibration and asymmetric stretching modes of oxalate, respectively. The other absorption peaks at 1313 and 1606 cm^{-1} represent $\nu_s(\text{COO})$ involving dangling oxygen atoms. Another two main peaks at 1471 and 1662 cm^{-1} correspond to $\nu_s(\text{COO})$ vibrations of oxalate. In addition, TGA of the pristine material in air was performed to check the stability of the sample (figure S3). The plot shows that the compound is stable up to 320 $^\circ\text{C}$.

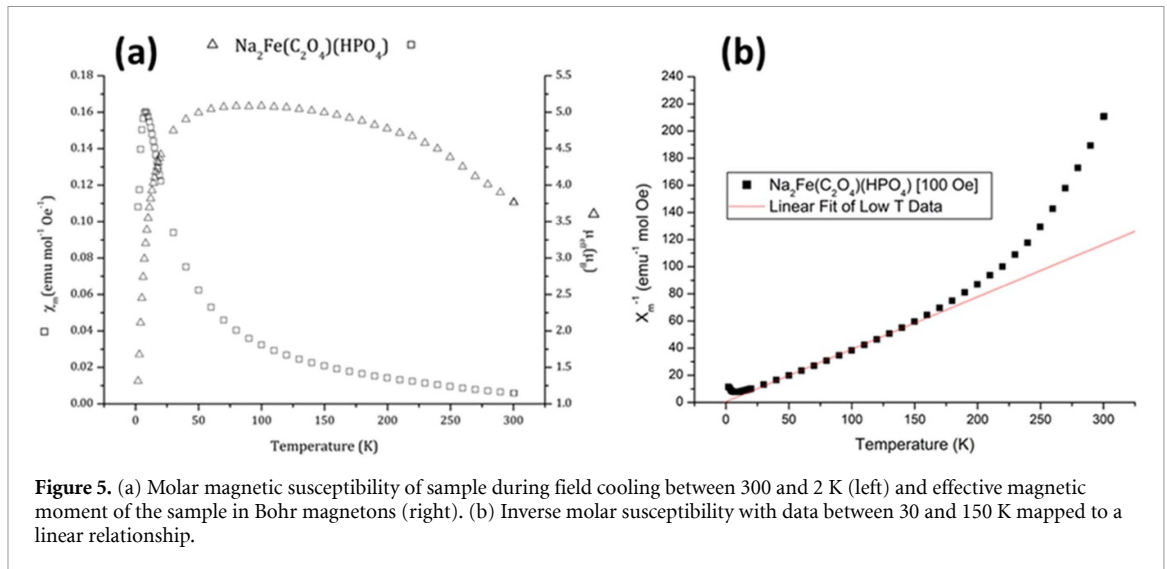


Figure 5. (a) Molar magnetic susceptibility of sample during field cooling between 300 and 2 K (left) and effective magnetic moment of the sample in Bohr magnetons (right). (b) Inverse molar susceptibility with data between 30 and 150 K mapped to a linear relationship.

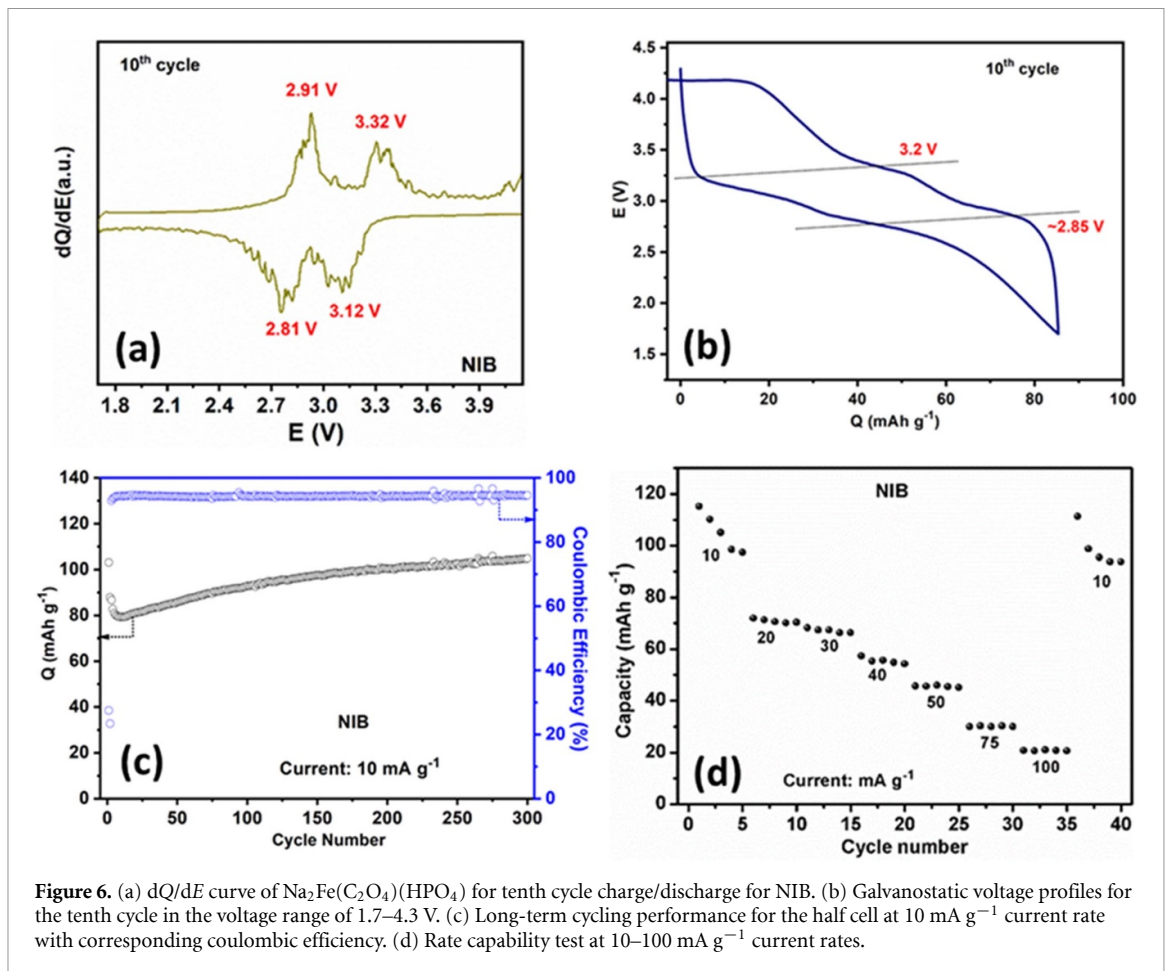


Figure 6. (a) dQ/dE curve of $\text{Na}_2\text{Fe}(\text{C}_2\text{O}_4)(\text{HPO}_4)$ for tenth cycle charge/discharge for NIB. (b) Galvanostatic voltage profiles for the tenth cycle in the voltage range of 1.7–4.3 V. (c) Long-term cycling performance for the half cell at 10 mA g⁻¹ current rate with corresponding coulombic efficiency. (d) Rate capability test at 10–100 mA g⁻¹ current rates.

3.2. Magnetic characterization

The magnetic susceptibility data are shown in figure 5. The value of the μ_{eff} at its plateau around 100 K (figure 5(a)) confirms the presence of solely Fe^{2+} ions in the structure (i.e. compatible with high spin d^6 , $S = 2$, $\mu_{\text{SO}} = 4.92 \mu_{\text{B}}$), with no evidence of significant impurity. The inverse susceptibility plot (figure 5(b)) suggests strong ferromagnetic (FM) interactions at high T , however a marked change of slope on cooling suggests a change to dominant antiferromagnetic (AFM) interactions below ~ 150 K, and a long-range ordered AFM state below ~ 10 K (figure 5(a)). It is possible that due to a variation of exchange pathways between magnetic ions within the crystal structure, FM clusters are initially formed which at lower temperature interact AFM. This AFM ordering seems rather weak, with a Weiss constant of -1.36 K

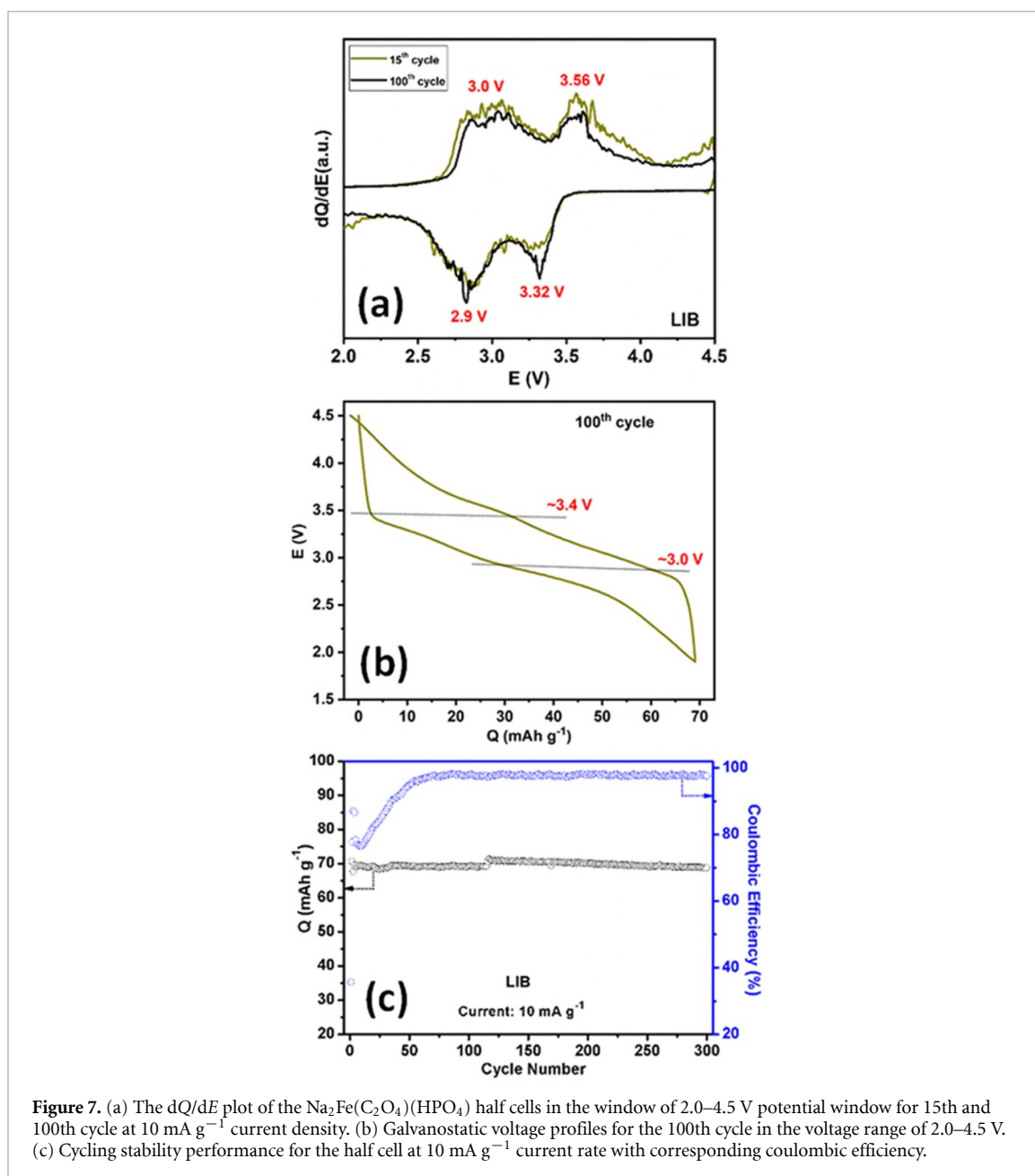


Figure 7. (a) The dQ/dE plot of the $\text{Na}_2\text{Fe}(\text{C}_2\text{O}_4)(\text{HPO}_4)$ half cells in the window of 2.0–4.5 V potential window for 15th and 100th cycle at 10 mA g^{-1} current density. (b) Galvanostatic voltage profiles for the 100th cycle in the voltage range of 2.0–4.5 V. (c) Cycling stability performance for the half cell at 10 mA g^{-1} current rate with corresponding coulombic efficiency.

calculated from the linear fit in figure 5(b), but is nonetheless sufficient to lead to a zero net moment below the transition temperature as the moments become fully compensated. A similar competition between FM and AFM correlations has previously been observed in $\text{La}_2\text{NiMnO}_6$ [26], although in that case the phenomenon was related to cation anti-site defects. Further studies are necessary to determine the precise mechanism in this case, which may be due to the enhanced structural complexity.

3.3. Electrochemical properties as battery cathode

3.3.1. Sodium-ion battery

In order to evaluate the electrochemical performance of $\text{Na}_2\text{Fe}(\text{C}_2\text{O}_4)(\text{HPO}_4)$, pellet electrodes were fabricated using a 60:30:10 weight % ratio of active material: carbon C65: PTFE binder with a typical active mass loading of ~ 7 – 8 mg . The typical dQ/dV plot of a stabilized half-cell cycled in the range of 1.7–4.3 V vs Na^+/Na at a rate of 10 mA g^{-1} for the tenth cycle, is displayed in figure 6(a). It reveals two distinct peaks at 2.91 V and 3.32 V during charge with corresponding peaks at 2.81 V and 3.12 V during discharge.

Figure 6(b) shows the voltage profile for the tenth cycle, with the corresponding two pairs of plateaus.

The long term cycling performance of $\text{Na}_2\text{Fe}(\text{C}_2\text{O}_4)(\text{HPO}_4)$ was evaluated at a rate of 10 mA g^{-1} in the potential window 1.7–4.3 V vs Na^+/Na , as shown in figure 6(c). The first cycle discharge capacity is $\sim 104 \text{ mAh g}^{-1}$, which gradually decreases for the first eight cycles before increasing and stabilizing at around $\sim 105 \text{ mAh g}^{-1}$ after 300 cycles. The initial cell polarization is relatively high for the first few cycles

before progressively decreasing, associated with the increase in reversible capacity. The Coulombic efficiency is low for the first few cycles before improving in subsequent cycles and reaches $\sim 95\%$. These observations are presumably associated with an electrochemical grinding effect on extended cycling which leads to improved contact between the grains and conducting carbon additive. The rate capability of $\text{Na}_2\text{Fe}(\text{C}_2\text{O}_4)(\text{HPO}_4)$ was evaluated at different current densities ($10\text{--}100\text{ mA g}^{-1}$) as shown in figure 6(d). At a current density of 10 mA g^{-1} , the capacity approached 96 mAh g^{-1} . Upon increasing the cycling rate, the reversible capacity progressively decreases. The average discharge capacities are $\sim 71, 67, 55, 46, 31$ and 21 mAh g^{-1} at rates of $20, 30, 40, 50, 75$ and 100 mA g^{-1} respectively. Once the rate was restored to the initial current density of 10 mA g^{-1} , the discharge capacity reached $\sim 94\text{ mAh g}^{-1}$, which indicates 98% restoration of the initial capacity.

3.3.2. Lithium-ion battery

$\text{Na}_2\text{Fe}(\text{C}_2\text{O}_4)(\text{HPO}_4)$ was also tested as a positive electrode for LIBs. Typically, galvanostatic charge–discharge experiments were performed in the potential window $2.0\text{--}4.5\text{ V}$ vs Li^+/Li at a rate of 10 mA g^{-1} . Figure 7(a) shows the dQ/dV plots for the 15th and 100th cycles. The lithiation/ delithiation of $\text{Na}_2\text{Fe}(\text{C}_2\text{O}_4)(\text{HPO}_4)$ shows two processes analogous with those observed when cycled vs sodium. The galvanostatic voltage profile for the 100th cycle corresponds to two plateaus with an average potential of $\sim 3.2\text{ V}$ (figure 7(b)). The two plateaus on charge/discharge are situated at $3.0/2.9\text{ V}$ and $3.56/3.32\text{ V}$ respectively, with an average voltage hysteresis of 0.15 V . This confirms a reversible electrochemical Li extraction/insertion process [27].

The performance of $\text{Na}_2\text{Fe}(\text{C}_2\text{O}_4)(\text{HPO}_4)$ on long-term cycling vs Li^+/Li was tested by constant galvanostatic charge/ discharge from 2.0 to 4.5 V at 10 mA g^{-1} , as shown in figure 7(c). The first cycle discharge capacity was $\sim 71\text{ mAh g}^{-1}$, corresponding to $\sim 76\%$ of its theoretical capacity. The coulombic efficiency was low for the first few cycles, before progressively increasing to $\sim 96\%$. Analogous to the behaviour observed in NIBs the cell polarisation decreases and Coulombic efficiency increases with cycle number. The material exhibits a very stable reversible capacity without fading up to 300 cycles. Note, we believe that further synthesis optimization, i.e. reducing the particle size, can significantly improve the electrochemical properties by obviating the electrochemical grinding process.

The PXRD patterns after 15 charge and discharge cycles are shown in figure S4. Although poorly crystalline it is apparent that there were no significant crystallographic changes during charge and discharge.

4. Conclusion

In this paper, we report the synthesis, electrochemical and structural characterization of a new insertion cathode for rechargeable lithium and sodium ion batteries. The naturally abundant Fe-based mixed polyanionic compound $\text{Na}_2\text{Fe}(\text{C}_2\text{O}_4)(\text{HPO}_4)$ was synthesised for the first time by hydrothermal means. The crystal structure was determined through SXRD, and phase purity was established by PXRD, magnetisation and elemental mapping. The electrochemical tests reveal stable reversible capacity, 71 mAh g^{-1} for LIB and 104 mAh g^{-1} for NIB, at average voltages of ~ 3.2 and $\sim 3.1\text{ V}$, respectively. The developing redox chemistry in mixed oxalate-phosphate polyanionic materials suggests that extensive opportunities exist to explore new low-cost, high-performance cathodes in this class of materials.

Acknowledgment

The authors thank EPSRC EP/R030472/1 for financial support.

Conflict of interest

The authors declare no competing financial interest.

ORCID iDs

Atin Pramanik  <https://orcid.org/0000-0002-3954-7770>

Alasdair J Bradford  <https://orcid.org/0000-0002-9952-0676>

Stephen L Lee  <https://orcid.org/0000-0002-2020-3310>

Philip Lightfoot  <https://orcid.org/0000-0001-7048-3982>

A Robert Armstrong  <https://orcid.org/0000-0003-1937-0936>

References

- [1] Yabuuchi N, Kubota K, Dahbi M and Komaba S 2014 Research development on sodium-ion batteries *Chem. Rev.* **114** 11636–82
- [2] Larcher D and Tarascon J M 2015 Towards greener and more sustainable batteries for electrical energy storage *Nat. Chem.* **7** 19–29
- [3] You Y, Kim S O and Manthiram A 2017 A honeycomb-layered oxide cathode for sodium-ion batteries with suppressed P3–O1 phase transition *Adv. Energy Mater.* **7**
- [4] Ding Y, Cano Z P, Yu A, Lu J and Chen Z 2019 Automotive Li-ion batteries: current status and future perspectives *Electrochem. Energy Rev.* **2** 1–28
- [5] Gao R M, Zheng Z J, Wang P F, Wang C Y, Ye H and Cao F F 2020 Recent advances and prospects of layered transition metal oxide cathodes for sodium-ion batteries *Energy Storage Mater.* **30** 9–26
- [6] Ali G, Lee J H, Susanto D, Choi S W, Cho B W, Nam K W and Chung K Y 2016 Polythiophene-wrapped olivine NaFePO₄ as a cathode for Na-ion batteries *ACS Appl. Mater. Interfaces* **8** 15422–9
- [7] Ni Q, Bai Y, Wu F and Wu C 2017 Polyanion-type electrode materials for sodium-ion batteries *Adv. Sci.* **4** 1600275
- [8] Manthiram A and Goodenough J B 1989 Lithium insertion into Fe₂(SO₄)₃ frameworks *J. Power Sources* **26** 403–8
- [9] Jin T, Li H, Zhu K, Wang P F, Liu P and Jiao L 2020 Polyanion-type cathode materials for sodium-ion batteries *Chem. Soc. Rev.* **49** 2342–77
- [10] Yao W, Sougrati M T, Hoang K, Hui J, Lightfoot P and Armstrong A R 2017 Na₂Fe(C₂O₄)F₂: a new iron-based polyoxyanion cathode for Li/Na ion batteries *Chem. Mater.* **29** 2167–72
- [11] Yeoh J S, Armer C F and Lowe A 2018 Transition metal oxalates as energy storage materials. A review *Mater. Today Energy* **9** 198–222
- [12] Yao W, Sougrati M T, Hoang K, Hui J, Lightfoot P and Armstrong A R 2017 Reinvestigation of Na₂Fe₂(C₂O₄)₃·2H₂O: an iron-based positive electrode for secondary batteries *Chem. Mater.* **29** 9095–101
- [13] Yao W et al 2019 An oxalate cathode for lithium ion batteries with combined cationic and polyanionic redox *Nat. Commun.* **10** 3483
- [14] Liu X, Tang L, Li Z, Zhang J, Xu Q, Liu H, Wang Y, Xia Y, Cao Y and Ai X 2019 An Al-doped high voltage cathode of Na₄Co₃(PO₄)₂P₂O₇ enabling highly stable 4 V full sodium-ion batteries *J. Mater. Chem. A* **7** 18940–9
- [15] Li Q, Lin B, Zhang S and Deng C 2016 Towards high potential and ultra long-life cathodes for sodium ion batteries: freestanding 3D hybrid foams of Na₇V₄(P₂O₇)₄(PO₄) and Na₇V₃(P₂O₇)₄@biomass-derived porous carbon *J. Mater. Chem. A* **4** 5719–29
- [16] Kim H et al 2015 Anomalous Jahn–Teller behavior in a manganese-based mixed-phosphate cathode for sodium ion batteries *Energy Environ. Sci.* **8** 3325–35
- [17] Senthilkumar B, Murugesan C, Sharma L, Lochab S and Barpanda P 2019 An overview of mixed polyanionic cathode materials for sodium-ion batteries *Small Methods* **3** 1800253
- [18] Yaghoobnejad Asl H and Choudhury A 2016 Combined theoretical and experimental approach to the discovery of electrochemically active mixed polyanionic phosphatonitrates, AFePO₄NO₃ (A = NH₄/Li, K) *Chem. Mater.* **28** 5029–36
- [19] Chen H, Hao Q, Zivkovic O, Hautier G, Du L S, Tang Y, Hu Y Y, Ma X, Grey C P and Ceder G 2013 Sidorenkite (Na₃MnPO₄CO₃): a new intercalation cathode material for Na-ion batteries *Chem. Mater.* **25** 2777–86
- [20] Song T, Yao W, Kiadkhunthod P, Zheng Y, Wu N, Zhou X, Tunmee S, Sattayaporn S and Tang Y 2020 A low-cost and environmentally friendly mixed polyanionic cathode for sodium-ion storage *Angew. Chem., Int. Ed.* **59** 740–5
- [21] Nagarathinam M, Saravanan K, Phua E J H, Reddy M V, Chowdari B V R and Vittal J J 2012 Redox-active metal-centered oxalato phosphate open framework cathode materials for lithium ion batteries *Angew. Chem., Int. Ed.* **51** 5866–70
- [22] Toby B H 2001 EXPGUI, a graphical user interface for GSAS *J. Appl. Crystallogr.* **34** 210–3
- [23] Farrugia L J 2012 WinGX and ORTEP for windows: an update *J. Appl. Crystallogr.* **45** 849–54
- [24] Von Dreele R B 1997 Quantitative texture analysis by Rietveld refinement *J. Appl. Crystallogr.* **30** 517–25
- [25] Yao W, Clark L, Xia M, Li T, Lee S L and Lightfoot P 2017 Diverse family of layered frustrated magnets with tailorable interlayer interactions *Chem. Mater.* **29** 6616–20
- [26] Zhou S M, Guo Y Q, Zhao J Y, Zhao S Y and Shi L 2010 Nature of short-range ferromagnetic ordered state above TC in double perovskite La₂NiMnO₆ *Appl. Phys. Lett.* **96** 262507
- [27] Kim H, Park I, Seo D H, Lee S, Kim S W, Kwon W J, Park Y U, Kim C S, Jeon S and Kang K 2012 New iron-based mixed-polyanion cathodes for lithium and sodium rechargeable batteries: combined first principles calculations and experimental study *J. Am. Chem. Soc.* **134** 10369–72